



Monitoring multi-temporal and spatial variations of water transparency in the Jiaozhou Bay using GOCI data

Yan Zhou^a, Dingfeng Yu^{a,b,*}, Wentao Cheng^c, Yingying Gai^a, Huiping Yao^d, Lei Yang^a, Shunqi Pan^b

^a Institute of Oceanographic Instrumentation, Qilu University of Technology (Shandong Academy of Sciences), Qingdao 266100, China

^b Hydro-Environmental Research Centre, School of Engineering, Cardiff University, Cardiff CF24 3AA, UK

^c Qingdao Institute of Bioenergy and Bioprocess Technology, Chinese Academy of Sciences, Qingdao 266101, China

^d College of Oceanography and Space Informatics, China University of Petroleum, Qingdao 266580, China

ARTICLE INFO

Keywords:

Coastal waters
Secchi disk depth
GOCI
Multiple variable linear regression
Environmental factors

ABSTRACT

Water transparency, commonly measured as Secchi disk depth (SDD), is essential for describing the optical properties of coastal waters. We proposed a regional linear corrected SDD estimation model based on the North Sea Mathematical Models for GOCI and the mechanical model developed by Lee et al. (2015) in the Jiaozhou Bay. Combined with the multiple variable linear regression analysis, the diurnal SDD variations of the bay inside and the bay mouth are controlled by the solar zenith angle (SZA) and tides. The bay outside mainly varies with SZA. From GOCI observations between 2011 and 2021, wind force influenced the entire area on the inner-annual SDD variations. It exhibits an increasing trend in the inter-annual dynamics, which was more stable inside the bay with an annual increase of 0.035 m, and air temperature was the most significant contribution. However, human activities cannot be ignored in causing water environment changes.

1. Introduction

As the transitional waters between ocean and land, the marine environment and ecosystem in the coastal water are easily affected by land, sea, and human development activities (Shanmugam et al., 2011), and the optical properties of water bodies are very complex (Ibrahim et al., 2018). As a common indicator of water quality evaluation (Aas et al., 2014), Water transparency quantified by Secchi disk depth (SDD) has been widely used in various countries for the management and monitoring of coastal water environments (Holland, 1993). Due to the simplicity and low cost, the SDD measurement plays a vital role in coastal hydrodynamic changes (Taillie et al., 2020), a load of water nutrients (Paerl et al., 2006), suspended sediments (Testa et al., 2019), and phytoplankton biomass (Kukushkin, 2014), and the primary productivity of underwater ecosystem (Gattuso et al., 2006). However, field measurement consumes a lot of workforce and material resources. The obtained data are discrete in time and space and have poor synchronization, which cannot meet the needs of real-time dynamic and long-term continuous observation of water bodies. Satellite remote sensing provides extensive area coverage in real-time with a short access cycle and

has become an essential means of water transparency monitoring (Alparslan et al., 2007; Dekker and Peters, 1993; N. Li et al., 2019).

The observation of water by satellite remote sensing technology is mainly carried out by polar orbit satellites equipped with optical sensors, such as Moderate Resolution Imaging Spectroradiometer (MODIS) (Harma et al., 2001; Menken et al., 2006; Ritchie et al., 1990), Landsat (Harrington et al., 1992; Lymburner et al., 2016; Pardo-Pascual et al., 2012), Sentinel-2 (Qing et al., 2021; Wang and Atkinson, 2018), etc. In the mid-latitudes, the repeated observation periods of satellites for the same region are at least half or one day, some reaching 16 days, which is far from meeting the demand for short-term dynamic observations of the coastal area. Compared with polar orbit satellites, geostationary orbit satellites can cover nearly a third of the Earth's area, achieve continuous observation of the same place and significantly improve the ability to monitor and evaluate coastal marine dynamics. In 2010, South Korea launched the world's first geostationary orbit ocean color satellite called Communication, Ocean & Meteorological Satellite (COMS). The earth synchronous ocean color imager (GOCI) boarded on COMS can obtain eight hourly observations every day that increased cloudless observation frequency. It covers the Bohai Sea, the Yellow Sea, and part of the East

* Corresponding author at: Institute of Oceanographic Instrumentation, Qilu University of Technology (Shandong Academy of Sciences), Qingdao 266100, China.
E-mail address: dfyu@qlu.edu.cn (D. Yu).

China Sea. It provides support for the SDD dynamic observation in coastal waters of China and the monitoring of related short-term marine phenomena (Doxaran et al., 2014), such as tides (Choi et al., 2014) and sea surface currents (Chen et al., 2019a).

In previous studies, the monitoring of the dynamic changes of water transparency in China has mainly focused on ecosystems of oceans (Chen et al., 2019b; He et al., 2017), inland lakes (Liu et al., 2021; Liu et al., 2020; Shen et al., 2020; Song et al., 2020), and rivers (Zhao et al., 2011). In terms of the driving factors of SDD spatial-temporal variation, the spatial distribution is related to the significant differences in water depth (Liu et al., 2020; Yin et al., 2021a) and altitude (Wang et al., 2020). From the time series perspective, the water components, such as chlorophyll-a, suspended particulate, and chromophoric dissolved organic matter, are the main factors causing underwater light penetration (Jia et al., 2018; Mao et al., 2018; Wu et al., 2009). The diurnal variation is primarily affected by the solar zenith angle (Mao et al., 2018) and tidal current (Shi et al., 2011). Seasonal and interannual variations are related to water stability dynamics (Bai et al., 2020; Kim et al., 2015; Mao et al., 2018) caused by multiple changes in runoff sediment (Ren et al., 2018; Zhao et al., 2021), wind speed (Shi et al., 2018; Zeng et al., 2020), rainfall (Li et al., 2021; Zhang et al., 2021), air temperature (Yin et al., 2021b; Zhang et al., 2014; Zhou et al., 2019), sea surface temperature (He et al., 2017), and average sunshine (Zhang et al., 2018), and combined effected by human activities such as gross domestic product (Wang et al., 2020), silt dredging (Jing et al., 2019), and water conservancy projects (Ren et al., 2018). However, the research on the contribution of each driving factor to SDD dynamic changes is not sufficient.

Water transparency variations are closely related to environmental conditions (Olmanson et al., 2008). We selected Jiaozhou Bay, a typical bay in northern China, to study the dynamic change mechanism of SDD in coastal waters. Only Yin et al. found that water depth and wind speed were essential factors affecting the spatial distribution and annual change of SDD in Jiaozhou Bay (Yin et al., 2021a). Then, how do environmental factors affect the SDD variations in coastal waters? What environmental factors have more extraordinary relative contributions to daily, monthly, and interannual variations, respectively? These are very important for studying the dynamic change mechanism of SDD in coastal waters. In this study, based on the in situ measurements, we

derived the multi-temporal and spatial scale SDD variations in Jiaozhou Bay from GOCI data between 2011 and 2021 and studied the relative contribution of each environmental factor, such as wind speed, rainfall, and air temperature, to the SDD dynamic change.

2. Data and methods

2.1. Study area

Jiaozhou Bay (36.06°–36.25°N, 120.10°–120.37°E) is located in Qingdao City on the south coast of the Shandong Peninsula of China. It connected with the Yellow Sea with the line between Tuandaotou and Xuejiadao and covered an area of 343.09 km². The average water depth is 7 m, and the shallow water area of 0–5 m accounts for 52.7% (Zhao et al., 2015), as shown in Fig. 1. The part on the east side is the granite low and gentle hilly bank. The north and northwest sides are sandy and muddy tidal flats formed by the sedimentation of seasonal rivers of Dagou River, Baisha River, and Yanghe that account for about 29.5% of the total area. The flood period of the rivers above concentrated in July, August, and September. It is a warm temperate monsoon climate zone, with northwesterly winds in Winter and southeasterly winds in Summer. The tide is a typical semi-diurnal. With the development of surrounding industries, Jiaozhou Bay and the adjacent Qingdao coastal waters have also become the main receptor for the discharge of land-based pollutants along the coastal area of Qingdao. Affected by coastal industrial pollution and sewage, it is easy to lead to poor water quality and concentrations rise of nutrient salts, and red tides are prone to occur (Xiao et al., 2007). The Jiaozhou Bay Sea-crossing Bridge constructed in 2011 has changed the original hydrodynamic environment of the sea area to a certain extent.

2.2. In-situ measurements

From 2016 to 2017, we conducted field surveys with the clear days and better sea conditions in Jiaozhou Bay. We obtained 30 sets of samples, including sea surface remote sensing reflectance spectrum and corresponding SDD. The hand-held Global Positioning System device recorded the locations (latitude and longitude) sampling sites. SDD is measured by a white disk that descended into the seawater until it

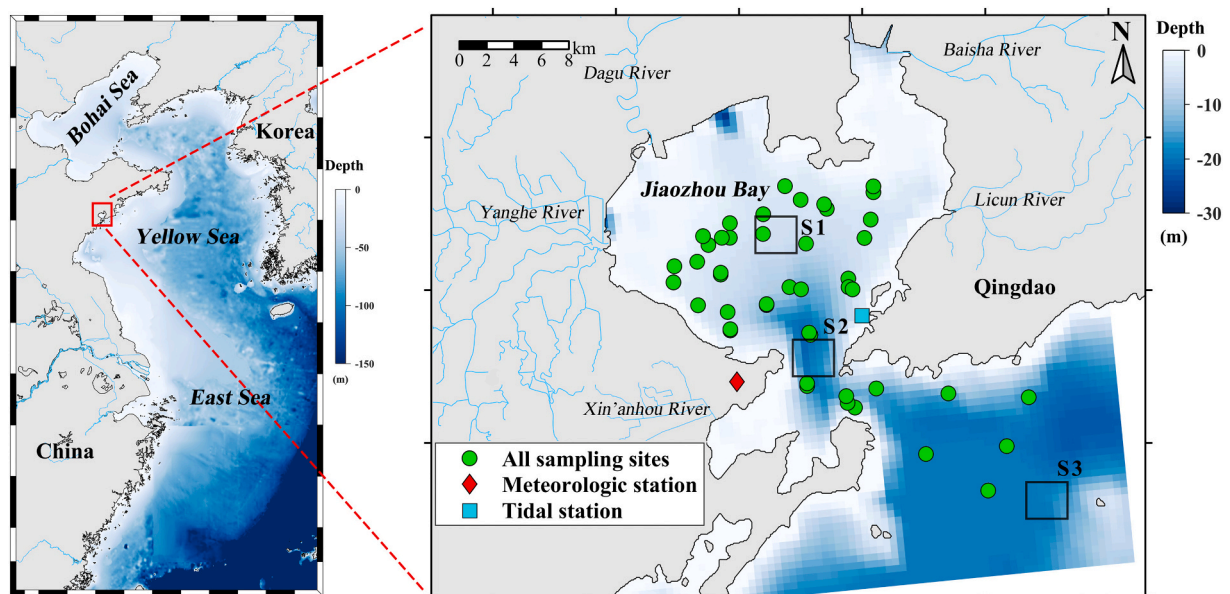


Fig. 1. The Jiaozhou Bay (JZB) bathymetry map overlaid with all sampling sites, meteorological station, and tidal station. The bathymetric data come from the ETOPO1–1 Arc-Minute Global Relief model. The subset study areas S1, S2, and S3 located at JZB inside, JZB mouth, and JZB outside, respectively, are outlined in the black box.

disappeared out of sight for this dataset. Referring to NASA's ocean optics protocols for biogeochemical and bio-optical measurements, we analyzed the synchronous collection of sea surface water samples in the laboratory and obtained the chlorophyll-a concentration (Chl-a), total suspended solids concentration (TSM), and absorption coefficient of chromophoric dissolved organic matter (CDOM) (Mueller et al., 2003). In addition, three cruises during 2018 were taken from the Jiaozhou Bay Marine Ecosystem Research Station (<http://jzb.cern.ac.cn/>) and got 24 sets of Secchi disk depth data. The location of all sampling sites is shown in Fig. 1, and the cruises covered four seasons in the year, as listed in Table 1.

According to the observation geometry with a zenith angle of 45° and an azimuth angle of 135° (Mobley, 1999), the upward radiance of the sea surface water ($L_{sw}(\lambda, 0^+)$), the sky light radiance ($L_{sky}(\lambda, 0^+)$), and the upward radiance of the reference panel ($L_p(\lambda, 0^+)$) are measured with high sensitivity spectrometer QE Pro (Ocean Insight Inc.). It has 1024 channels between 195.0 nm to 955.0 nm. To ensure the quality of spectral data, each parameter at the sampling sites is taken 50 times measurements that spanning at least one wave cycle. In the case of avoiding direct solar reflection, ignoring or avoiding water surface bubbles, the remote sensing reflectance (R_{rs}) is derived:

$$R_{rs}(\lambda) = \frac{\rho_p(\lambda)(L_{sw}(\lambda, 0^+) - r \times L_{sky}(\lambda, 0^+))}{\pi L_p(\lambda, 0^+)} \quad (1)$$

where $\rho_p(\lambda)$ is the direction-hemispheric reflectance of the standard diffuse reflector, r is the reflectance of the air-water interface. After the process of dark noise correction, air-water interface reflectance determination, and abnormal data removal, the remote sensing reflectance spectrum above the sea surface are calculated from Eq. (1) and then resampled to simulate the GOCI equivalent remote sensing reflectance spectra of each waveband according to the spectral response function of GOCI sensor. This study used 23 of 30 samples matching the measured R_{rs} data.

2.3. GOCI data collection and processing

The remote sensing dataset we used in this study is GOCI Level 1B data from 1 April 2011 to 31 March 2021, downloaded from Korea Ocean Satellite Center (KOSC <http://kosc.kiost.ac.kr/>). Each daily GOCI data collected is centered at 412, 443, 490, 555, 660, 680, 745, and 865 nm, with a spatial resolution of 500 m and high-temporal frequency (eight observations from 8:16 to 15:16 in local time at a frequency of 1 h). Using GOCI Data Processing System (GDPS, Version 2.0) distributed by KOSC, L1B data are browsed and cropped. As for complex properties of turbid coastal water in Jiaozhou Bay, the Management Unit of the North Sea Mathematical Models (MUMM) embedded in GDPS software is used for atmospheric correction. It replaced the assumption of the zero radiance in the near-infrared band in the open ocean sea surface with the spatial homogeneity in the aerosol reflectivity and the water-leaving reflectivity of the study area (Ruddick et al., 2000). We use this model to generate a Level 2 remote sensing reflectance product in this study. When performing spatial-temporal matching with the in-situ dataset, the time window of GOCI images is ± 0.5 h, and the spatial window is 3 pixels \times 3 pixels.

Table 1
Summary of field surveys to measure ocean properties in this study.

Season	Cruise	Number of Samples				
		R_{rs}	SDD	Chl-a	TSM	CDOM
Spring	16 May 2017	15	15	15	15	15
	9 March 2018	–	8	–	–	–
Summer	20 June 2018	–	8	–	–	–
Autumn	2 November 2016	15	15	15	15	15
Winter	12–13 December 2018	–	8	–	–	–
Total		30	54	30	30	30

He et al. (2021) demonstrated that the Level 2 sea surface water-leaving radiance products obtained by GDPS performed well at observation times of 02, 03, and 04, but less so at observation times of 00, 01, 05, 06, and 07 with the relative error to the field measurements exceeding 100%, which is not acceptable in the process of data use (He et al., 2021). Therefore, when studying the variations in the time series of months and years, we only select the daily observation time data of 02, 03, and 04 to be included in the statistical analysis.

2.4. Environmental and socio-economic data

Meteorological data of Qingdao coastal area were recorded by Qingdao meteorological station (Fig. 1), such as 24-hour average wind speed (m/s), daily cumulative precipitation (mm), and air temperature ($^\circ\text{C}$). These data during 2011 and 2020 were obtained from the China Meteorological Data Service Center (<http://data.cma.cn/>) and processed to different time scales. Notably, precipitation is accumulated by month and year, and wind speed and air temperature are averaged by month and year. Hourly tidal height data were provided by the National Marine Data and Information Service (<http://global-tide.nmdis.org.cn/>). The yearly statistical data of industrial wastewater discharged (10,000 tons) between 2011 and 2019 were extracted from the Qingdao statistical yearbook. The Grade I and II waters proportion data during 2015 and 2019 was simultaneously obtained.

2.5. SDD retrieval models

To exactly represent the physical processes of sighting of a disk in a waterbody by human eyes, the new underwater visibility theory developed by Lee et al. (2015) (hereafter called Lee_2015 model) is used to estimate the visibility in the vertical direction (Lee et al., 2015). It is modeled with the diffuse attenuation coefficient (K_d) and corresponding R_{rs} and expressed as follows:

$$SDD_{Lee} = \frac{1}{2.5 \text{Min}(K_d^{tr})} \ln \left(\frac{|0.14 - R_{rs}^{tr}|}{0.013} \right) \quad (2)$$

where $\text{Min}(K_d^{tr})$ is the minimum K_d in the visible waveband (412, 443, 490, 555, 660, 680 nm) of the GOCI sensor, R_{rs}^{tr} is the remote sensing reflectance corresponding to the waveband with the minimum K_d value. The diffuse attenuation coefficient K_d at each waveband of GOCI can be obtained from the semi-analytical model of the inherent optical properties (particularly for total absorption and backscattering coefficients) of the water column and solar zenith angle developed by Lee et al. (2005, 2013). Thus, the key to retrieving water transparency is to obtain total absorption (a) and backscattering coefficients (b_b) of the water from the GOCI Level 2 product. In this study, we adopted the quasi-analytical algorithm (QAA, version 6.0) to derive a and b_b of the water when accurate R_{rs} data are available (Lee et al., 2002).

In contrast with empirical methods, the semi-analytical models generally do not require in-situ measurement data to recalibrate the inversion model. Previous field survey dataset in coastal and open waters of China and the USA with SDD values ranging between ~ 0.1 and 30 m has proved an excellent performance of the Lee_2015 model with an absolute difference of $\sim 18\%$. Therefore, the Lee_2015 model appears robust enough without re-parameterization of the model coefficients when applied to various satellite remote sensing data. Because of the complex properties of turbid coastal water in Jiaozhou Bay, it is unlikely to be optimal for all regions, and it becomes necessary to introduce an empirical relation into the Lee_2015 model (Feng et al., 2019). The linear correction equation is as follows:

$$SDD_{corr} = a_0 \times SDD_{Lee} + a_1 \quad (3)$$

where a_0 and a_1 are the slope and intercept of the linear equation.

2.6. Regression analysis and accuracy assessment

Regression analysis is a statistical process used to evaluate the relationship between the independent variable X and the dependent variable Y . The linear trend obtained from the least square fitting is used for the single variable regression of the observational factors change with time (Bradley et al., 2007). Multiple variable linear regression (MVLRL) is applied to compare the relative contributions of different parameters in water transparency variation (Forootan et al., 2016). When using multivariate statistical analysis, it is necessary to quantify each variable into a unified unit to standardize all variables, including the dependent variable, normalize each variable matrix to the [0,1] range, and then perform linear regression. The regression coefficient obtained can show the importance of the corresponding independent variable, and the absolute value of the coefficient reflects the degree of influence (relative contribution) of the independent variable X on the dependent variable Y . It is expressed as:

$$y = b_0 + b_1x_1 + b_2x_2 + \dots + b_kx_k + \varepsilon \quad (4)$$

where $b_0 \dots b_k$ are regression parameters, ε is the random error. In regression analysis, P -value from the t -test is used to test the significance of each regression parameter in the regression model.

Due to limited numbers of SDD samples matched with GOCI images, we adopt the leave-one-out cross-validation (LOOCV) method to verify the performance of the model developed by the linear fitting relationship (Feng et al., 2015). The LOOCV method takes all samples but one sample data to train the model and use the leaving one to perform the accuracy of the inversion model assessment. All samples of the matches were looped to get the regression coefficient of each cross-validation model. The weighted average of the error size between the measured and estimated value is used to get the final regression model. Compared with the traditional method of randomly dividing the original sample into training data sets and test set according to a certain proportion, the LOOCV method has the highest representativeness of the samples. It eliminated the potential impact of outliers in the limited sample data set on the algorithm's accuracy through cumbersome calculation.

As to evaluate the accuracy of the atmospheric correction and inversion model, three statistical parameters, including the determination coefficient (R^2), root means square error (RMSE), and mean absolute percentage error (MAPE) are used in this study. The equations are as follows:

$$RMSE = \sqrt{\frac{\sum_{i=1}^N (x_{est,i} - x_{mea,i})^2}{N}} \quad (5)$$

$$MAPE = \frac{1}{N} \sum_{i=1}^N \left(\frac{|x_{est,i} - x_{mea,i}|}{x_{mea,i}} \right) \times 100\% \quad (6)$$

where, $x_{est,i}$ is the estimated value from GOCI observation, $x_{mea,i}$ is the corresponding matched field measured value; N is the number of matched samples between the data of GOCI derived and in-situ measured.

3. Results

3.1. Water components characteristics

The field survey carried out on 2 November 2016 and 16 May 2017 included both water transparency and water component parameters data from all the survey measurements. The in-situ data of these two days was selected to obtain the variations of water quality in Jiaozhou Bay, including the chlorophyll-a concentration (mg/m^3), the suspended particulate matter concentration (mg/L), and the absorption coefficient of colored soluble organic matter at 400 nm (m^{-1}). All these parameters can be used as an indicator standard to measure the eutrophication

condition of the water. As shown in Table 2 of the summary of the data of two days, SDD ranged from 0.7 m to 2.5 m, Chl-a concentration ranged from $0.785 \text{ mg}/\text{m}^3$ to $5.190 \text{ mg}/\text{m}^3$, TSM concentration was varied between 1.6 mg/L and 45.3 mg/L , and $a_{\text{CDOM}}(400)$ has coverage of 0.162–0.553 m^{-1} . Referring to the classification of water body types by the water component coefficients, the results in Table 2 indicate that the water body of Jiaozhou Bay is approximately a low, moderate turbid water ($1 < \text{TSM} < 50$) (Yu et al., 2019), and the eutrophic state is oligotrophic ($\text{Chl-a} < 10 \text{ mg}/\text{m}^3$, $a_{\text{CDOM}}(400) < 1 \text{ m}^{-1}$) (Shang et al., 2021). Through the correlation analysis between the daily measured and all the statistical results of the two days, SDD and three water components are both negatively correlated. The increased concentration of each water component will significantly reduce the light transmittance of the water layer and the vertical visibility. Among them, statistics of two field surveys show that the total correlation between TSM and SDD was the highest ($R = -0.576$), followed by Chl-a ($R = -0.483$), and CDOM was the lowest ($R = -0.411$), but the correlation coefficients obtained by the three were not much different. It shows that the water transparency of Jiaozhou Bay is greatly affected by the suspended sediment in the water. Suspended sediment may come from a seasonal influx of runoff, terrigenous sediment brought in by precipitation, and sediment resuspension at the bottom of the water body caused by wind force on the sea surface.

3.2. Validation using field measurements

3.2.1. Performance of atmospheric correction

In the time window of $\pm 0.5 \text{ h}$, the scatter plot of the R_{rs} data between the atmospheric correction result from the GOCI L1B data by the GDPS MUMM module and the equivalent waveband data of the in-situ measured are presented in Fig. 2. The corresponding statistical results are shown in Table 3.

As shown in Fig. 2, the atmospheric correction performance of the MUMM model is good, and the amplitude of each R_{rs} waveband is relatively consistent with the measured data. From Table 3, the blue waveband (412, 443, and 490 nm) is better and obtains better R^2 statistics ($R^2 > 0.6$), the green waveband (555 nm) is a little weaker ($R^2 = 0.40$), and the red waveband (660 nm and 680 nm) is poor ($R^2 = 0.18$). In comparison, the near-infrared waveband (745 nm) has increased ($R^2 = 0.47$), but the deviation is more significant ($\text{RMSE} = 0.0048 \text{ sr}^{-1}$, $\text{MAPE} = 58.04\%$), and the fitting degree of all the above wavebands is statistically significant (P -value < 0.05). Since the atmospheric correction results in the 865 nm band have a low correlation ($R^2 < 0.1$) and insignificant trend (P -value > 0.05) with the measured data, they are not shown in the scatterplot. After taking the obtained fitting slopes and intercepts of each waveband, the R_{rs} data from GOCI derived was linearly corrected as the input of the subsequent inversion model.

3.2.2. Adjustment of SDD algorithm

After inputting the GOCI-corrected R_{rs} data into the QAA algorithm and the Lee_2015 model, their SDD output was compared with the matched field-measured SDD values. The LOOCV method is used with the matching samples to cross-validate the linear fitting model. The LOOCV results are shown in a scatter plot of measured and estimated SDD, as shown in Fig. 3. The scatter plot data are distributed on both sides of the 1:1 line. Most data (32 of 38) are distributed within the $\pm 10\%$ RE line, and a small part of the data locates between the $\pm 10\%$ RE line and the $\pm 20\%$ RE line. From accuracy assessment, it exhibits high R^2 ($R^2 = 0.76$) and low deviation ($\text{RMSE} = 0.36 \text{ m}$, $\text{MAPE} = 21.28\%$). It indicated that the linear correction model has a high accuracy of SDD values with the field-measured. After LOOCV method, the Lee_2015 model is linearly corrected, and fitting coefficients are $a_1 = 0.893$, $a_2 = 0.614$.

Table 2

Descriptive statistics and correlation analysis between Secchi disk depth and water components were measured in-situ. Here, SD is standard deviation, CV is coefficient of variation, and correlation statistics refers specifically to the Pearson correlation coefficient between two datasets.

Date	Statistics	SDD (m)	Chl-a (mg/m ³)	TSM (mg/L)	a _{CDOM} (400) (m ⁻¹)
2 November 2016	Min-Max	1.10–2.50	0.785–5.190	1.600–11.200	0.184–0.553
	Average ± SD	1.77 ± 0.36	1.887 ± 1.435	5.680 ± 2.579	0.308 ± 0.110
	CV	0.205	0.761	0.457	0.356
	Correlation	–	–0.432	–0.431	–0.393
16 May 2017	Min-Max	0.70–2.00	1.910–4.130	3.400–45.300	0.162–0.460
	Aver ± SD	1.14 ± 0.43	3.169 ± 0.712	21.837 ± 16.352	0.327 ± 0.087
	CV	0.375	0.225	0.748	0.267
	Correlation	–	–0.395	–0.626	–0.551
Total correlation	–	–	–0.483	–0.576	–0.411

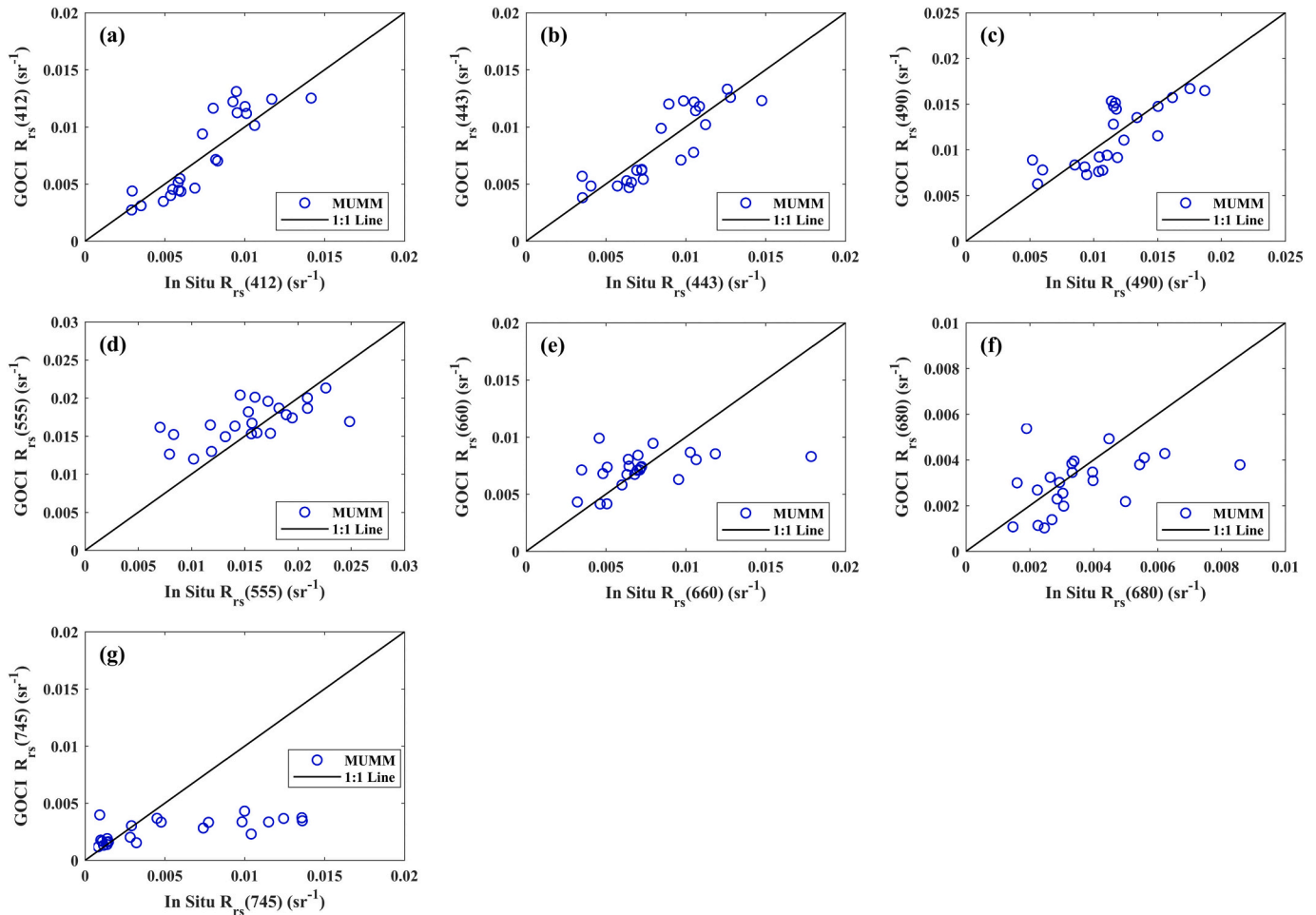


Fig. 2. Scatterplots of GOCI retrieved remote sensing reflectance (R_{rs}) using GDPS MUMM module versus the waveband equivalent of the in situ R_{rs} . (For interpretation of the references to color in this figure, the reader is referred to the web version of this article.)

3.3. SDD variations in Jiaozhou Bay mapped by GOCI data

3.3.1. Spatial pattern

From the GOCI products from 1 April 2011 to 31 March 2021, the SDD spatial distribution map of the entire study area was obtained after atmospheric correction and model inversion, as shown in Fig. 4. From the spatial distribution of the annual average and standard deviation images, the overall transparency of the sea area is low (0–4 m). It shows a gradually increasing trend from the inside to the outside of the bay. The variance varies from 0 to 2 m. The water depth in the coastal area inside the bay is generally less than 10 m, and the water transparency is low. The northern part of the bay is a typical breeding area, rich in organic matter, and industrial pollution and domestic sewage along the

northwest and east coasts of the bay bring rich nutrients to the bay. The nutrient of the seawater is lower on the sea surface than on the bottom layer and significantly higher inside the bay than outside the bay (Ren et al., 1999). Due to the large water depth in the central area of the bay and the bay mouth, the water bodies frequently exchange between the bay inside and outside, so the water transparency here is high. The transparency of some areas outside the bay is not as high as that at the bay mouth, mainly attributed to the strong scattering characteristics of the coastal water.

3.3.2. Diurnal variation

We selected three days of GOCI images on 22 March, 28 April, and 29 April, and accumulated 24 SDD images at different times through

Table 3

Statistical results for GOCI-retrieved R_{rs} values obtained from the GDPS MUMM module (independent variable) and the waveband equivalent of the in-situ R_{rs} (dependent variable). The slope and intercept give a linear relationship between the changes in the independent and dependent variables above.

Wavelength (nm)	R^2	RMSE (sr^{-1})	MAPE (%)	Slope	Intercept	P-value
412	0.78	0.0017	20.98	0.684	0.0023	<0.01
443	0.75	0.0016	18.57	0.791	0.0019	<0.01
490	0.61	0.0023	18.92	0.779	0.0026	<0.01
555	0.40	0.0038	24.42	1.167	-0.0041	<0.01
660	0.18	0.0028	27.08	0.898	0.0008	<0.05
680	0.18	0.0017	37.06	0.596	0.0018	<0.05
745	0.47	0.0048	58.04	3.171	-0.0029	<0.01
865	0.04	0.0523	74.94	-23.201	0.0989	>0.05

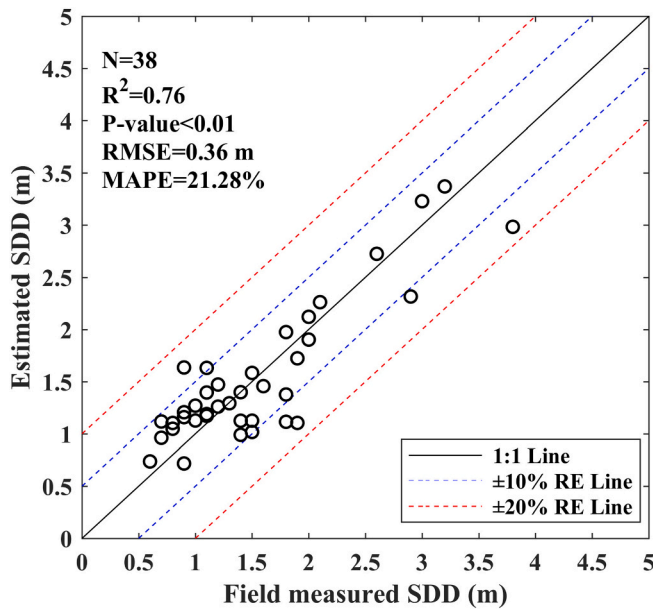


Fig. 3. Scatter plot of field-measured and estimated SDD matching in Jiaozhou Bay computed by the leave-one-out cross-validation (LOOCV) method.

remote sensing inversion, as shown in Figs. 5–7. Subplot (a) to (h) shows the daily spatial distribution of water transparency from 8:16 to 15:16 local time in the Jiaozhou Bay. Under the hourly observation of the GOCI sensor, the water transparency in Jiaozhou Bay changes every day, and it shows a trend of low in the morning and evening and high at noon in the entire sea area. Low-transparency areas ($SDD < 1.5$ m, shown as red patches) gradually shrink into the bay inside before 12:16 at noon (subplot (a)–(d)), high-transparency areas ($SDD > 2.5$ m, shown as blue patches) gradually expand out of the bay after 12:16 at noon. Water transparency is directly related to the penetration characteristics of light in water, so water transparency hourly observations from the GOCI sensor are inevitably affected by the solar zenith angle (SOLZ) (H. Li et al., 2019). It varies significantly from early morning to later afternoon, detailed with the highest in the early morning and later afternoon and the lowest at noon, which is exactly opposite with the change of water transparency. The tidal current in the Qingdao coastal area is a regular semi-diurnal tidal current (Li et al., 2014). Because of the shallow water depth in the coastal zones, the water exchanges caused by the tide fluctuation will directly lead to the variation of water components in different water layers. Affected by the solar zenith angle and tides, the changes in different regions of the Jiaozhou Bay are not the same. To further quantify the diurnal variations in different regions, we selected three representative areas, namely, the JZB inside (S1), the JZB mouth (S2), and the JZB outside (S3), respectively, to statistics the 8-hour changes of the GOCI-derived SDD, and to compare them with the daily solar zenith angle and tidal height, as shown in subplot (i).

From the tidal information of each day, we found that the low water (54 cm) took place at 10:30 AM on 22 March 2020, after which the tidal height began to rise. The high water on April 28 and 29 was 8:00 AM and 8:50 AM, respectively. After that, the tides fell for 6.5 h and then reached the lowest tides, which was almost the last time of the GOCI observation of the day. We can qualitatively analyze the influence on water transparency variations through the changes of tidal height and the solar zenith angle at each moment of these three days. Comparing the daily change curves of water transparency, the peak value in the bay outside (S3) approximately coincides with the time of the minimum value of the solar zenith angle. Whether in the period of tides rising or falling or low water occurring at noon, the water transparency in the bay outside still reaches the maximum value around 12:16 AM. It shows that the water transparency in the bay outside is mainly affected by the solar zenith angle.

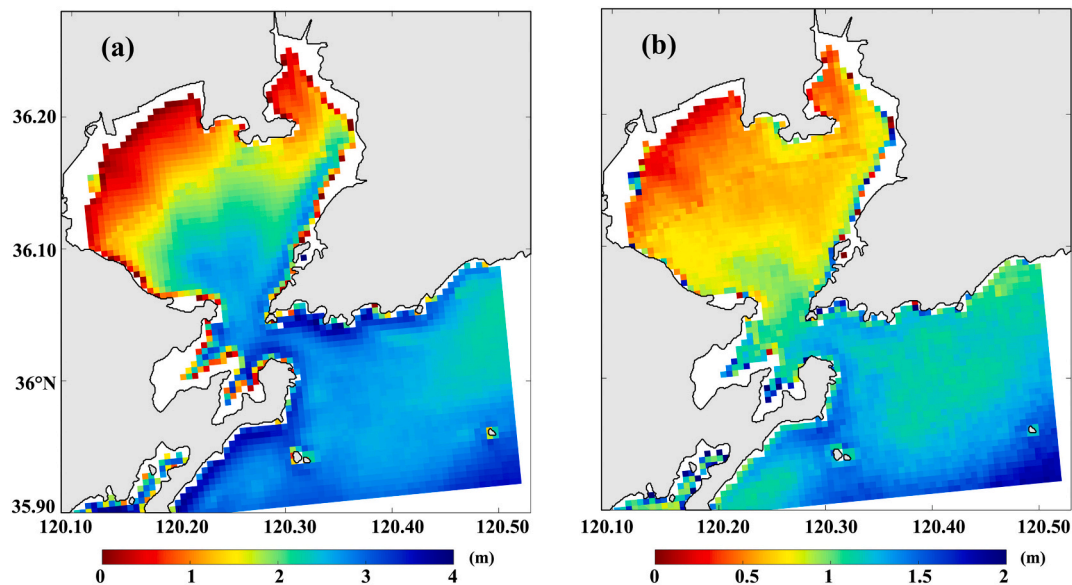


Fig. 4. The spatial distribution image of annual average (a) and corresponding standard deviation (b) of Secchi disk depth (SDD) data from GOCI-derived from 1 April 2011 to 31 March 2021.

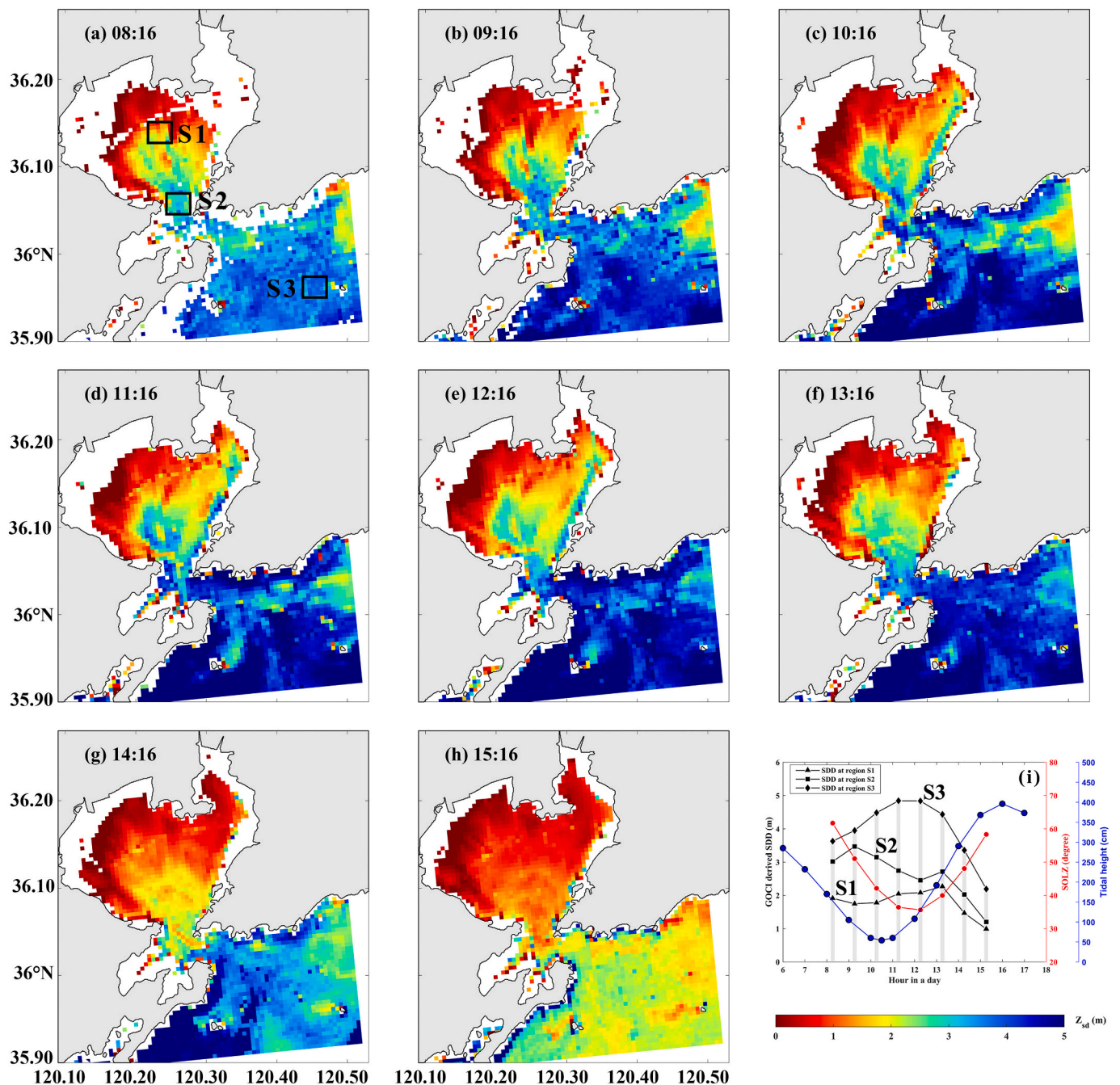


Fig. 5. Hourly sea surface GOCI-derived SDD on 22 March 2020 from 8:16 to 15:16. The last panel shows 8-hour variations of GOCI-derived SDD at three regions around JZB and their comparisons with diurnal solar zenith angel and tidal height. Region S1, S2, and S3 are located at JZB inside, JZB mouth, and JZB outside, respectively. Tidal height data were from the National Marine Data Information Center.

As for the variations of the bay mouth, what increased with the solar zenith angle in the early morning of 22 March, reaching the maximum value at 9:16 AM, and then gradually decreased in the period of the tide falling. However, the solar zenith angle still fell, and the tidal height began to rise slowly after 10:30 AM. Under the dual action of the solar zenith angle and the tide, there was a brief rise at 13:16 and a rapid decline. On April 28 and 29, the GOCI observation time was basically during the period of the falling tide. Although the tidal height kept falling, the water transparency did not decline during the morning.

In the case of the bay inside, the water transparency decreased slightly at 9:16 AM on 22 March, then raised slowly during the morning, and reached a peak value at 13:16. Although the solar zenith angle is no longer the lowest value of the day, the tidal height is at the time of rapid

rise. On 28 April, the peak value appeared at 10:16 AM, and it has been decreasing since then. On 29 April, the transparency slowly increased to 11:16 AM and then reduced. Compared to the environmental condition of 28 and 29 April, the solar zenith angle is nearly the same, but only the time of high water on the two days differed by 50 min. So, the different observation time of peaks value that appeared inside the bay may be caused by the difference in tidal height. Due to the shallow water depth in this area, when a low tidal height level happens, lower than 200 cm, the water transparency dynamics may be controlled by the tide to a great extent than the solar zenith angle.

Multiple linear regression analysis was used to quantitatively analyze the relative contribution of solar zenith angle and tide to the change of transparency in each region, as shown in Table 4. The absolute

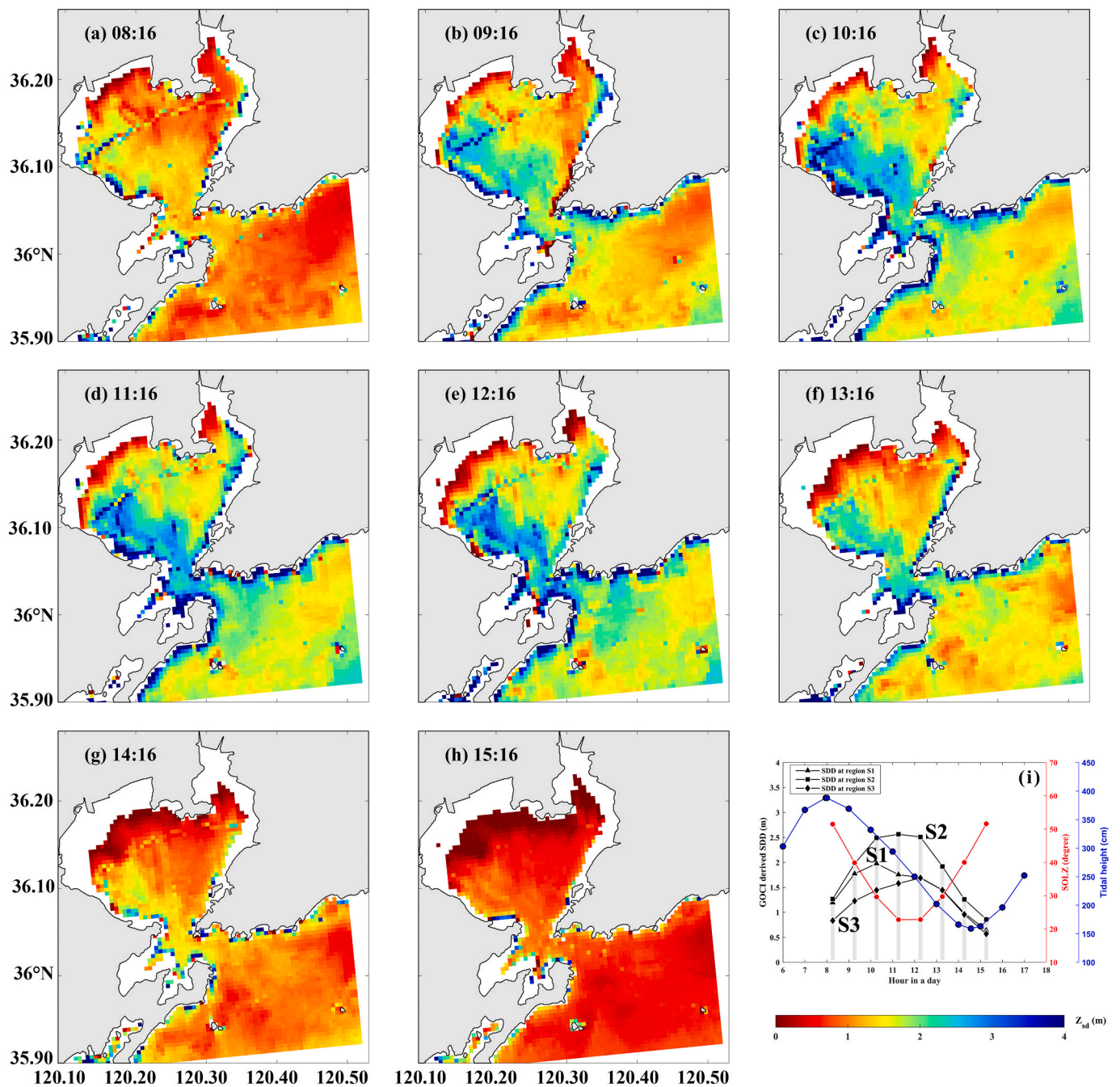


Fig. 6. Same as Fig. 5, but for 28 April 2020.

value of the regression coefficient was used to judge the relative contribution of each factor. After statistical analysis, the regression coefficients of the solar zenith angle in the bay outside (S3) are the largest of the three, which also shows to a certain extent that the main effect factor of the transparency variations in the bay outside is the solar zenith angle. The regression coefficients of the solar zenith angle and tidal height obtained from the bay mouth (S2) and the bay inside (S1) cannot determine which factors have the most significant contribution. Therefore, the changes in water transparency in these two areas are affected by the combined effect of the solar zenith angle and the tidal height. According to the above analysis inside the bay, the contribution of tides on variations of water transparency of this region is more significant.

3.3.3. Monthly variations

Fig. 8 shows monthly mean SDD variations of JZB inside (region S1),

JZB mouth (region S2), and JZB outside (region S3) from 2011 to 2021. From the monthly SDD average values in various regions, there is little change in each month at the bay inside, and the peak value is reached in May. The bay mouth and outside area showed prominent variation characteristics of higher in Summer (June to August) and lower in Winter (December to February). The peak value occurs in May at the bay mouth, in August at the bay outside, and the minimum took place in December. It means that the entire area of Jiozhou Bay is in the lowest water transparency in Winter, which is related to the highest solar zenith angle compared with other seasons. For the variation of monthly average water transparency, the range is 1.74–2.62 m at the bay inside, 1.5–3.6 m at the bay mouth, and 1.2–4.0 m at the bay outside.

The dynamic changes of water transparency are closely related to the seasonal changes of meteorological factors on the sea surface. According to the statistical data of the average wind speed, cumulative

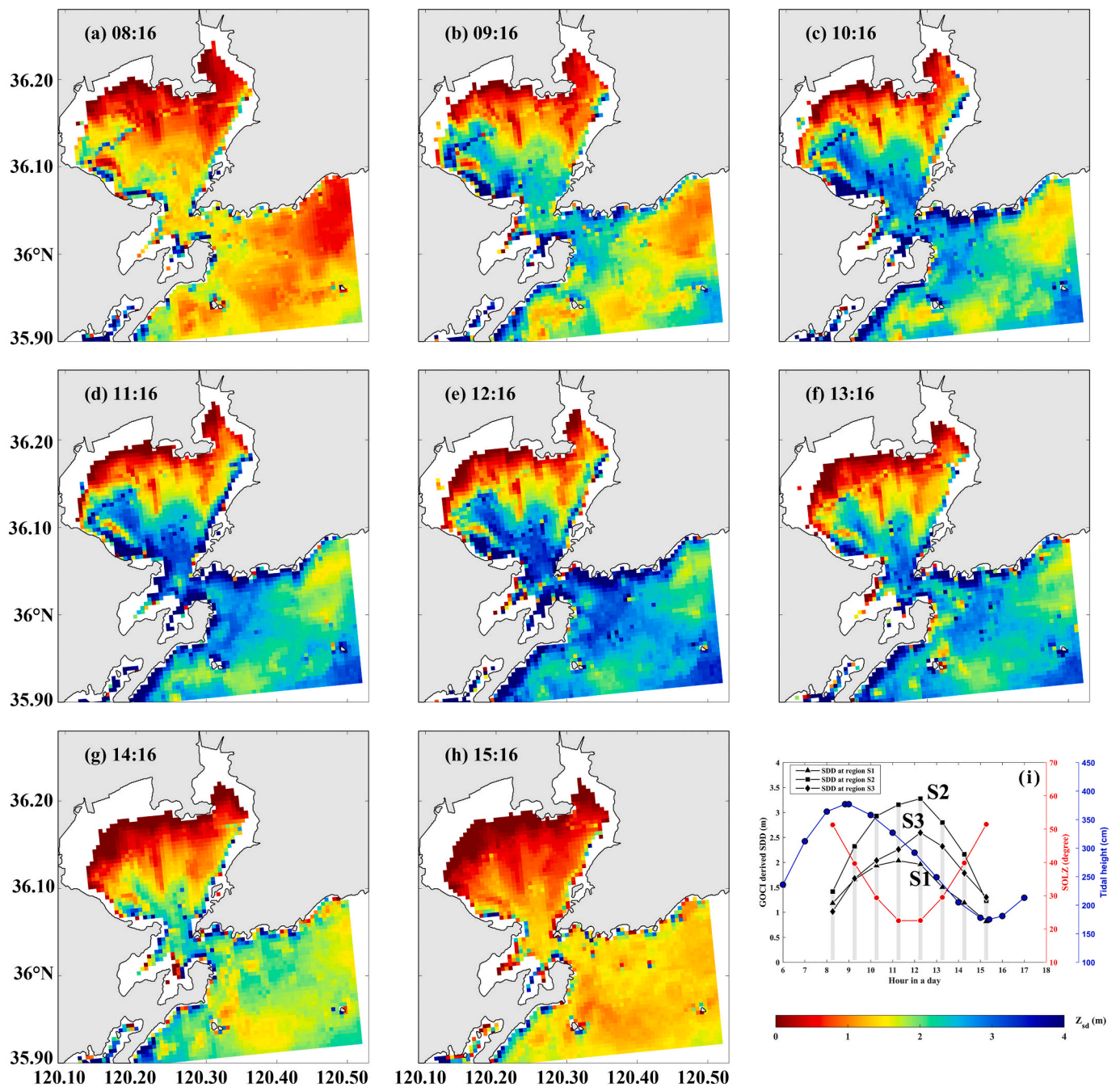


Fig. 7. Same as Fig. 5, but for 29 April 2020.

precipitation, and air temperature of each month, the wind speed is higher than 3.5 m/s from November to April and lower in another month. The rainfall is more in summer (174 mm in July and 135 mm in August), and lower in other months (lower than 70 mm). The air temperature is high in Summer (28.18 °C in August) and low in Winter (0.73 °C in January). Fig. 9 shows the single-factor correlation analysis of the monthly average SDD in each region with each meteorological factor. The monthly SDD is negatively related to wind speed and positive with precipitation and air temperature. In contrast, SDD at the bay mouth and inside had a higher correlation with air temperature, while SDD at the bay outside had a slightly stronger correlation with precipitation. According to the regression coefficient from the multivariate linear analysis listed in Table 5, the absolute value of the regression coefficient of the wind speed obtained in each area is the largest, and the trend is significant (P -value < 0.05). It shows that wind force generally

makes the most significant contribution to the monthly variation of water transparency in the entire Jiaozhou Bay area.

3.3.4. Inter-annual variations

Taking the entire sea area inside of the bay mouth as the area of Jiaozhou Bay inside, and the area outside the bay mouth as the sea area outside the bay, the long-term variations of the annual average SDD values of the two areas were statistically analyzed during 2012 and 2020 when full data in all months was available, as shown in Fig. 10(a). Related influence factors are presented in Fig. 10(b) and (c), including meteorological factors (wind speed, cumulative precipitation, and air temperature) and human activities (industrial wastewater discharged and the proportion of Grade I and II waters).

In general, the water transparency of the entire Jiaozhou Bay has shown an increasing trend from 2012 to 2020. The rising trend of

Table 4

Multiple linear regression is applied to determine the relationships between the SDD dynamics and the influence factors around three regions. Referring to Eq. (4), b_0 , b_1 , and b_2 are regression parameters, x_1 and x_2 correspond to the solar zenith angle and tidal height, respectively.

Date	Region	Multiple linear regression				
		b_0	b_1	b_2	R^2	P-value
22 March 2020	S1	1.008	-0.390	-0.486	0.703	<0.05
	S2	0.940	0.103	-0.869	0.825	<0.01
	S3	1.093	-0.512	-0.493	0.910	<0.01
28 April 2020	S1	0.644	-0.677	0.541	0.945	<0.01
	S2	0.815	-0.864	0.330	0.992	<0.01
	S3	0.877	-0.856	0.218	0.970	<0.01
29 April 2020	S1	0.764	-0.794	0.395	0.986	<0.01
	S2	0.906	-0.859	0.118	0.984	<0.01
	S3	1.038	-0.849	-0.197	0.965	<0.01

Jiaozhou Bay inside was stable ($R^2 = 0.794$, P -value = 0.001) with an annual increase of about 0.035 m, which was consistent with the changing trend of the proportion of Grade I and II waters recorded in the statistical yearbook of Qingdao, as shown in Fig. 10(c). The water transparency of the Jiaozhou Bay outside also increased, but it was not significant ($R^2 = 0.093$, P -value = 0.423). Compared with the annual average wind speed data and cumulative precipitation, the inter-annual variation is relatively close, but the correlation with the SDD inter-annual dynamics is not high. As seen in Fig. 10(b), compared with 2012, both the precipitation and wind speed decreased in 2013, but the decreasing extent in precipitation was more significant, and the transparency only decreased slightly. The relative contribution of rainfall to the reduction of transparency is larger. Compared with 2015, both wind speed and precipitation increased in 2016, but the water transparency still decreased. Currently, the relative contribution of wind speed is slightly more significant. From a comprehensive analysis, wind speed and precipitation can affect changes in water transparency variations,

but they are not the main factors affecting long-term changes. The annual mean air temperature data from 2011 to 2020 show a particular increase, coinciding with SDD dynamics. Combined with the multiple linear regression analysis results given in Table 6, the relative contribution of air temperature is the largest in the entire Jiaozhou Bay area. Still, not all the regression trend of each region is statistically significant (P -value > 0.05). Compared with the variations in water transparency driven by meteorological factors, we cannot ignore human activities in the changes in the water environment. From the total industrial pollution discharge from 2011 to 2019 (Fig. 10(c)), the industrial wastewater discharged in Qingdao City has been decreasing year by year, which is conducive to the improvement of water quality along the Jiaozhou Bay and the promotion of a virtuous circle of the ecological environment in the bay.

4. Discussion

4.1. Uncertainties of the remotely sensed SDD

In this study, the remote sensing reflectance products obtained from atmospheric correction of GOCI images are used to estimate the water transparency of Jiaozhou Bay. For remotely sensed SDD, the uncertainty mainly comes from two aspects: the performance of the atmospheric correction model and the application of the inversion model. We use field measured R_{rs} data to correct the result from the atmospheric correction and take the measured SDD to calibrate the Lee_2015 model. The algorithm calibrated based on the Lee_2015 model uses the minimum K_d value of the visible light range and the remote sensing reflectance of the corresponding waveband to participate in the calculation. The minimum K_d value in the Jiaozhou Bay area is concentrated in the blue bands. From Fig. 2, the remote sensing reflectance data in the blue wavebands fit well with the measured ($R^2 > 0.6$). By linear correction with the measured R_{rs} data, it can make the estimate of SDD relatively

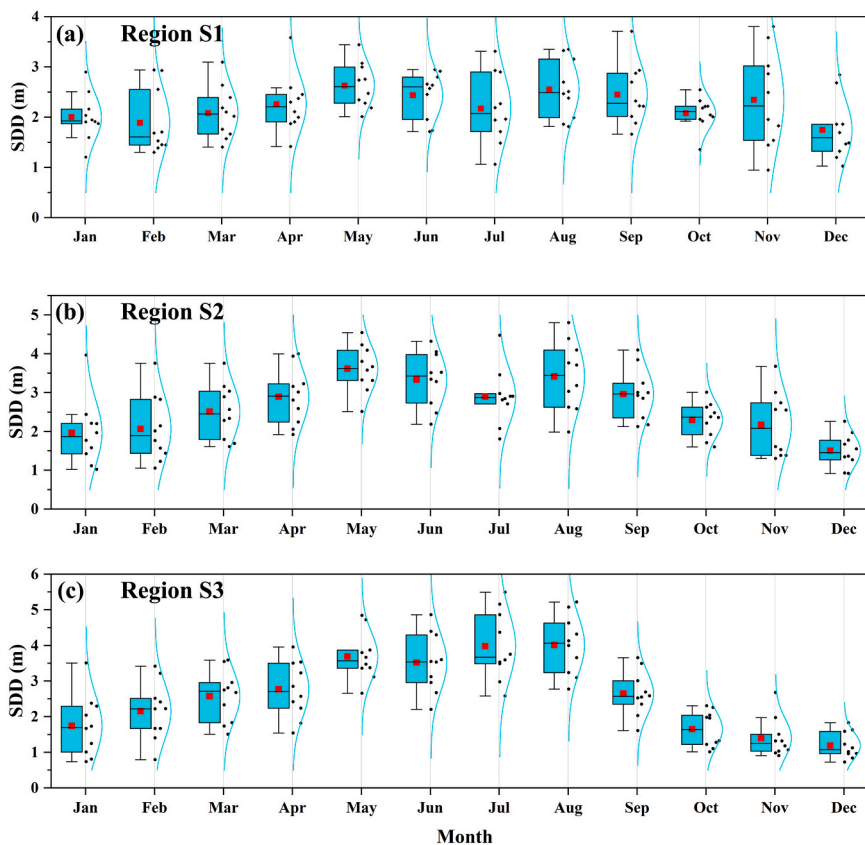


Fig. 8. Monthly SDD variations of JZB inside (a), JZB mouth (b), and JZB outside (c). Each boxplot chart includes the minimum, maximum, median, first quartile, third quartile, outliers, and mean value (red square). Each boxplot's right is a normal distribution of current month data from 2011 to 2021, including the distribution range of the scatter points (black dots) and the standard distribution curve (cyan lines). (For interpretation of the references to color in this figure legend, the reader is referred to the web version of this article.)

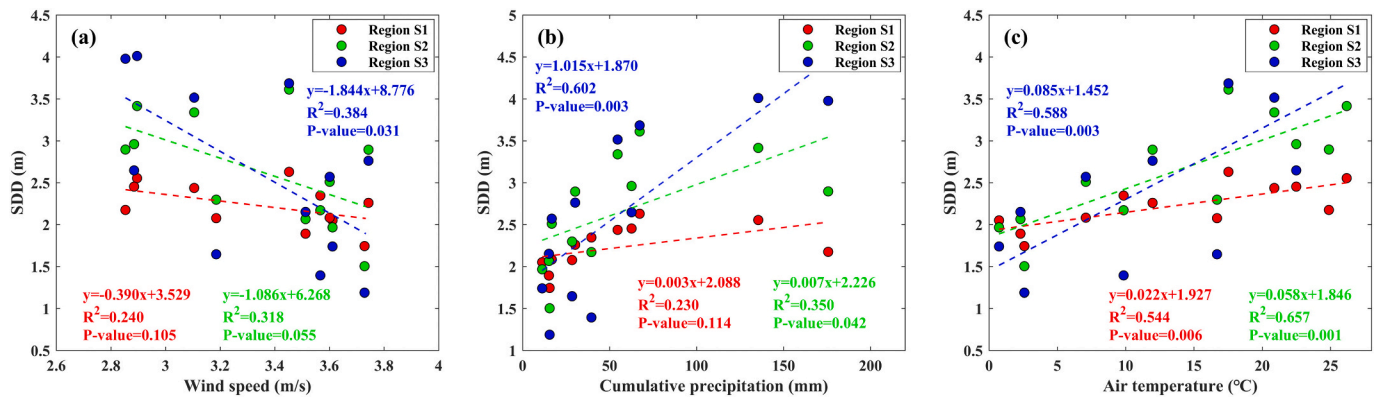


Fig. 9. The relationship between the monthly SDD of region S1, S2, and S3 and monthly mean meteorological factors, including wind speed (a), cumulative precipitation (b), and air temperature (c) from 2011 to 2021. The dashed line represents the trend of the fitted monthly variation.

Table 5

Multiple linear regression is applied to determine the relationships between the monthly SDD dynamics of each region (S1, S2, and S3) and the influence of meteorological factors around three areas. In Eq. (4), b_0 , b_1 , b_2 , and b_3 are regression parameters, x_1 , x_2 , and x_3 correspond to the wind speed, cumulative precipitation, and air temperature, respectively.

Region	Multiple linear regression					
	b_0	b_1	b_2	b_3	R^2	P-value
S1	0.284	0.469	-0.068	0.437	0.661	0.027
S2	0.272	0.478	-0.022	0.429	0.747	0.008
S3	0.313	0.343	0.187	0.237	0.688	0.020

accurate. It is worth noting that there is still high uncertainty in the GOCI atmospheric correction under high solar zenith angle conditions (Li et al., 2020). In addition, due to the strong scattering of suspended particles in turbid water, the K_d value may be overestimated when applying the QAA model, resulting in an underestimation of SDD (Bowers et al., 2020). The SDD estimated seems to be generally lower than the field measured value (Fig. 3), and the correlation between the two data groups can be used to correct the SDD estimation.

The uncertainty of the remotely sensed SDD may also be caused by the accumulated systematic errors from the quality of the field measurement dataset and the estimation model of the optical parameters of the water body. Many semi-analytical models are applied to estimate the inherent optical properties of the water, such as QAA_v5 (Lee et al., 2009), QAA_M14 (Mishra et al., 2014), QAA_V (Joshi and D'Sa, 2018), and QAA_hybrid (Jiang et al., 2019), and many empirical and semi-analytical models are used to obtain K_d from satellite remote sensing observations (Cao et al., 2014; Chen et al., 2015; Lee et al., 2005). Therefore, we need more field-measured data in the future to evaluate and verify the validity and applicability of remote sensing inversion models in Jiaozhou Bay.

4.2. Driving force for SDD variations

4.2.1. Water components

In the coastal waters, the changes in water transparency can reflect the changes in the aquatic ecological environment and terrestrial input. The penetration and attenuation of light underwater are closely related to the water optical components (chlorophyll *a*, suspended particulate matter, chromophoric dissolved organic matter). Due to the significant weight difference of each optical component in different water bodies, water transparency is the combined effect of all water components on underwater light (Gattuso et al., 2006).

As a good indicator of marine phytoplankton biomass and primary productivity, the empirical relationship between chlorophyll-*a* and

water transparency is primarily determined by the covariation between chlorophyll-*a* concentration and total suspended particles (Tilzer, 1988). The biomass of phytoplankton directly affects the attenuation of light in water and reduces solar radiation penetration, manifesting as a decrease in water transparency. The increase of suspended particulate concentration in water will enhance the diffusion of underwater light and change the spectral quality of the underwater light field (Brewin et al., 2015). Especially in turbid coastal and inland waters, the attenuation of light in water is mainly contributed by the high scattering characteristics of suspended particles (Sun et al., 2009; Sun et al., 2010). As a light absorption substance, the CDOM absorption in the range of blue light will inhibit the photosynthesis of phytoplankton, especially in coastal and estuary waters with high turbidity and high organic matter content. Moreover, these optical components do not change the underwater light field independently. Such as, the sedimentation and transportation of inorganic particles hinder the circulation of nutrients, and the high suspension of particulate substances in water also brings about the high carrying of nutrients (Hakanson and Blenckner, 2008), which also impairs the photosynthesis of phytoplankton to some extent.

4.2.2. Solar zenith angle and tide

Observation geometry under time change impacts the ocean color remote sensing detection of geostationary orbit marine satellites. Because there is a strong negative correlation between SDD and K_d , and Kirk found a positive correlation between K_d and SOLZ (Kirk, 1984), particularly obvious in clear water. Relative to the water inside the bay, the water transparency at the bay mouth and outside are clearer and easier to be affected by SOLZ. The size of the solar zenith angle directly reflects the change of solar height, that is, the change of light propagation length in water (Pitarch, 2020). It is worth noting that when the solar zenith angle is less than 50°, the variation of atmospheric parameters is slight. When the solar zenith angle is greater than 50°, the relative deviation caused by the angle of the blue light band increases rapidly, which directly leads to the worst performance of the atmospheric correction model in the early morning and late morning. In comparison, the relative deviation of other bands begins to increase rapidly only after the solar zenith angle is greater than 60°, which is caused by the high reflectivity of turbid water in these bands (Sun et al., 2017). From Figs. 5–7, we can see the information of solar zenith angles at different times. On 22 March, the degree of solar zenith angles observed by GOCI at 8:16, 9:16, and 15:16 in Jiaozhou Bay was greater than 50°. On April 28 and 29, the degree of solar zenith angles observed in the morning and evening (8:16 and 15:16) was greater than 50°, which may also be an essential factor causing the low transparency in the early morning and late evening from model inversion.

The tidal current is the primary source of water power. The effect of tide on the water environment is manifested in promoting sediment transport and nutrient cycling, intensifying vertical mixing of the water

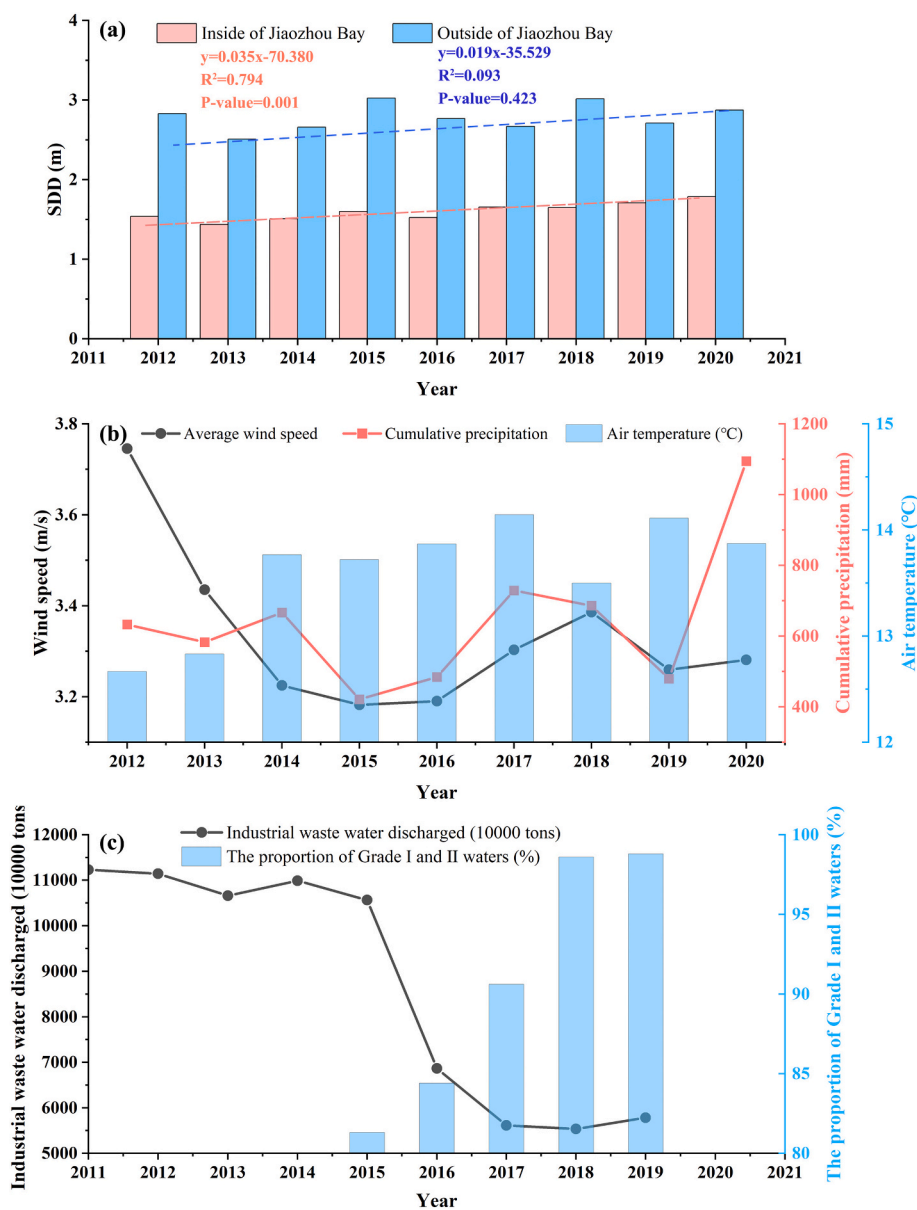


Fig. 10. Long-term trends in the annual mean GOCI-derived SDD values of Jiaozhou Bay inside (red histogram) and Jiaozhou Bay outside (blue histogram) from 2012 to 2020 (a), and variations of related meteorological factors (wind speed, cumulative precipitation, and air temperature) (b) and human activities (industrial wastewater discharged and the proportion of Grade I and II waters) (c). The dashed line represents the trend of the fitted interannual variation from 2011 to 2020. (For interpretation of the references to color in this figure legend, the reader is referred to the web version of this article.)

Table 6

Multiple linear regression is applied to determine the relationships between the long-term SDD dynamics of Jiaozhou Bay inside and Jiaozhou Bay outside and the influence factors. In Eq. (4), b_0 , b_1 , b_2 , and b_3 are regression parameters, x_1 , x_2 , and x_3 correspond to the wind speed, annual cumulative precipitation, and air temperature, respectively.

Region	Multiple linear regression					
	b_0	b_1	b_2	b_3	R^2	P-value
Inside of Jiaozhou Bay	-0.279	0.592	0.117	0.935	0.697	0.091
Outside of Jiaozhou Bay	0.418	0.078	0.111	0.015	0.014	0.994

body, and driving the resuspension of bottom particles (Cheng et al., 2016). The tidal current in Jiaozhou Bay is mainly reciprocating flow with high rising tide velocity, low falling tide velocity, corresponding short rising tide time, and long falling tide time (Li et al., 2014). In the flow process of pollutants from the coast and runoff and nutrients in the aquaculture area, the eddy mixing of seawater dominates (Liu et al.,

2005). The water depth in the bay is shallow, and pollutants and nutrients drift along the tidal current direction, so the short-term dynamic change of water transparency at the bay inside is driven by the tidal current.

It is worth noting that water depth has the most significant impact on water transparency in coastal waters. The change of tidal height directly affects the change of water depth in coastal waters. The shallower water depth area is located at the bay mouth or the estuary of runoff. With the increase of wind speed, the bottom water vortex with rich nutrients is agitated to rise, which supports the growth of phytoplankton. The seabed silt is accessible to resuspension under the influence of waves and currents so that the concentration of suspended particles is increased. Compared with coastal waters, the water characteristics of each water layer in open oceans with deep waters are relatively stable, and the water transparency is less driven by wind force.

4.2.3. Meteorological factors

Meteorological factors causing the change of water quality factor concentration in water, such as wind speed, rainfall, and air temperature, can indirectly lead to the dynamic change of water transparency.

Wind forces can drive the resuspension of substances at the bottom of the water body and increase the concentration of suspended particulate matter in the water body, which plays an essential role in the coastal waters and inland lakes (Capuzzo et al., 2015). According to the scatter plot analysis in Fig. 9, SDD was significantly positively correlated with rainfall and air temperature in terms of seasonal variation of SDD. Increased precipitation transports land-based sediment and nutrients to coastal waters through rivers, but the filtering of turbid waters by surrounding vegetation seems to counteract these effects on water transparency and dilute the original coastal turbid waters (Hou et al., 2017). Precipitation mainly affects seasonal changes in transparency but contributes less to long-term changes over many years (Song et al., 2015). It can be seen from Fig. 8 that the changing trend of transparency in each season is consistent with that of air temperature. In the past 30 years, the air temperature in Jiaozhou Bay has risen gently, which has brought about an increase in sea surface temperature (Zhang et al., 2019). All that enhanced the photosynthesis of phytoplankton and accelerated the absorption of nutrients in the water. From the results of multiple variable linear regression in Table 5, the relative contribution of air temperature to the long-term change of water transparency in Jiaozhou Bay was the largest, but not significant (P -value > 0.05).

4.2.4. Human activities

Human activities have an essential impact on the water environment dynamics in Jiaozhou Bay. Compared with the bay outside, the water transparency at the bay inside shows a stable increasing trend year by year (Fig. 10). Yin et al. noted that changes in water transparency were mainly concentrated in coastal areas and relatively small in the central region (Yin et al., 2021a). That is because coastal areas are more susceptible to human activities, and the most direct manifestation is the discharge of industrial wastewater. According to the statistical yearbook of Qingdao from 2011 to 2019, the total discharge of industrial wastewater scaling by 10,000 tons decreased from 1122.975 in 2011 to 577.999 in 2019. It is shown that the improvement of water quality in the Qingdao coastal area is noticeable, and the proportion of Grade I and II waters increased from 81.3% in 2015 to 98.8% in 2019.

In addition, since the completion of the Jiaozhou Bay Bridge in early 2011, it has affected the hydrodynamic environment of Jiaozhou Bay and further blocked the spread of sea ice to the south, resulting in serious ice accretion in the northern bay (Huang et al., 2019). The piles of the cross-sea bridge weaken the hydrodynamic environment on the north side of the bridge, changing the convective diffusion of suspended solids and sediment transport, and blocking the transport of seasonal freshwater from runoff to the open ocean. It would improve the water transparency of the bay but aggravate the ice condition in winter.

5. Conclusion

In this study, we evaluate the performance of the MUMM atmospheric correction model embedded in GDPS and the Lee_2015 model that is applied to remotely sensed SDD in the Jiaozhou Bay. The results from these two models are corrected using the in situ measured data to improve the accuracy of SDD estimation results. It shows that the R_{rs} data obtained from the atmospheric correction model is highly correlated with the measured data in the blue light band, and the R^2 between the SDD correction model and the measured data reaches 0.75. The calibration model generates the hourly SDD map to study the region's multi-temporal and spatial scale change of characteristics. The multiple variable linear regression model quantifies the relative contribution of environmental factors to the SDD changes.

It is found that GOCI is adequate for effective mapping the short-term SDD distributions in the Jiaozhou Bay. Hourly maps show that the diurnal variations of SDD at the bay inside and the bay mouth are affected by the combined effect of the solar zenith angle and tides, but the solar zenith angle is the main factor to influence the SDD outside the bay. In the entire bay, monthly SDD variations vary with wind force, and

an increasing trend is shown in the inter-annual dynamics, among which a clear rising trend in the bay of an annual increase of 0.035 m. Although the relative contribution of air temperature on the long-term SDD changes is the largest, human activities also play an essential part in changing the water environment at the study site.

Due to the complex optical properties of Class II water bodies, more in situ measurement data needs to be supplemented. Meanwhile, the calibration of satellite products for high solar zenith angle observations in the early morning and late afternoon requires further research to improve the accuracy of remote sensing dynamics monitoring.

CRediT authorship contribution statement

Yan Zhou: Conceptualization, Investigation, Formal analysis, Visualization, Writing – original draft, Writing – review & editing. **Dingfeng Yu:** Conceptualization, Resources, Writing – review & editing, Funding acquisition. **Wentao Cheng:** Resources, Visualization. **Yingying Gai:** Formal analysis, Writing – review & editing. **Huiping Yao:** Investigation, Resources. **Lei Yang:** Resources. **Shunqi Pan:** Writing – review & editing.

Declaration of competing interest

The authors declare that they have no known competing financial interests or personal relationships that could have appeared to influence the work reported in this paper.

Acknowledgements

This work was supported by the National Natural Science Foundation of China (42106172), State Key Laboratory of Tropical Oceanography, South China Sea Institute of Oceanology, Chinese Academy of Sciences (LTO2017), State Key Laboratory of Estuarine and Coastal Research (SKLEC-KF202001), the Natural Science Foundation of Shandong (ZR2019PD021), and the Foundation of Institute of Oceanographic Instrumentation, Shandong Academy of Sciences (HYPY202107).

References

- Aas, E., Hokedal, J., Sorensen, K., 2014. Secchi depth in the Oslofjord-Skagerrak area: theory, experiments and relationships to other quantities. *Ocean Sci.* 10, 177–199.
- Alparslan, E., Aydoğan, C., Tufekci, V., Tufekci, H., 2007. Water quality assessment at Ömerli Dam using remote sensing techniques. *Environ. Monit. Assess.* 135, 391.
- Bai, S.Y., Gao, J.X., Sun, D.Y., Tian, M.R., 2020. Monitoring water transparency in shallow and eutrophic lake waters based on GOCI observations. *Remote Sens.* 12, 163.
- Bowers, D.G., Roberts, E.M., Hogue, A.M., Fall, K.A., Massey, G.M., Friedrichs, C.T., 2020. Secchi disk measurements in turbid water. *J. Geophys. Res. Oceans* 125, e2020JC016172.
- Bradley, B.A., Jacob, R.W., Hermance, J.F., Mustard, J.F., 2007. A curve fitting procedure to derive inter-annual phenologies from time series of noisy satellite NDVI data. *Remote Sens. Environ.* 106, 137–145.
- Brewin, R.J.W., Sathyendranath, S., Muller, D., Brockmann, C., Deschamps, P.Y., Devred, E., Doerffer, R., Fomferra, N., Franz, B., Grant, M., Groom, S., Horseman, A., Hu, C., Krasemann, H., Lee, Z., Maritorena, S., Meelin, F., Peters, M., Platt, T., Regner, P., Smyth, T., Steinmetz, F., Swinton, J., Werdell, J., White, G.N., 2015. The ocean colour climate change initiative: III. A round-robin comparison on in-water bio-optical algorithms. *Remote Sens. Environ.* 162, 271–294.
- Cao, F., Fichot, C.G., Hooker, S.B., Miller, W.L., 2014. Improved algorithms for accurate retrieval of UV/visible diffuse attenuation coefficients in optically complex, inshore waters. *Remote Sens. Environ.* 144, 11–27.
- Capuzzo, E., Stephens, D., Silva, T., Barry, J., Forster, R.M., 2015. Decrease in water clarity of the southern and central North Sea during the 20th century. *Glob. Chang. Biol.* 21, 2206–2214.
- Chen, J., Zhu, Y.L., Wu, Y.S., Cui, T.W., Ishizaka, J., Ju, Y.T., 2015. A neural network model for K(λ) retrieval and application to global K-par monitoring. *PLoS ONE* 10, e0127514.
- Chen, J., Chen, J.Y., Cao, Z.Y., Shen, Y., 2019a. Improving surface current estimation from geostationary ocean color imager using tidal ellipse and angular limitation. *J. Geophys. Res. Oceans* 124, 4322–4333.
- Chen, J., Han, Q.J., Chen, Y.L., Li, Y.D., 2019b. A Secchi depth algorithm considering the residual error in satellite remote sensing reflectance data. *Remote Sens.* 11, 1948.

- Cheng, Z.X., Wang, X.H., Paull, D., Gao, J.H., 2016. Application of the geostationary ocean color imager to mapping the diurnal and seasonal variability of surface suspended matter in a macro-tidal estuary. *Remote Sens.* 8, 244.
- Choi, J.K., Park, Y.J., Lee, B.R., Eom, J., Moon, J.E., Ryu, J.H., 2014. Application of the Geostationary Ocean Color Imager (GOCI) to mapping the temporal dynamics of coastal water turbidity. *Remote Sens. Environ.* 146, 24–35.
- Dekker, A.G., Peters, S.W.M., 1993. The use of the Thematic Mapper for the analysis of eutrophic lakes: a case study in the Netherlands. *Int. J. Remote Sens.* 14, 799–821.
- Doxaran, D., Lamquin, N., Park, Y.-J., Mazeran, C., Ryu, J.-H., Wang, M., Poteau, A., 2014. Retrieval of the seawater reflectance for suspended solids monitoring in the East China Sea using MODIS, MERIS and GOCI satellite data. *Remote Sens. Environ.* 146, 36–48.
- Feng, L., Hu, C., Han, X., Chen, X., Qi, L., 2015. Long-term distribution patterns of chlorophyll-a concentration in China's largest freshwater lake: MERIS full-resolution observations with a practical approach. *Remote Sens.* 7, 275–299.
- Feng, L., Hou, X.J., Zheng, Y., 2019. Monitoring and understanding the water transparency changes of fifty large lakes on the Yangtze Plain based on long-term MODIS observations. *Remote Sens. Environ.* 221, 675–686.
- Forootan, E., Khandu, Awange, J.L., Schumacher, M., Anyah, R.O., van Dijk, A.I.J.M., Kusche, J., 2016. Quantifying the impacts of ENSO and IOD on rain gauge and remotely sensed precipitation products over Australia. *Remote Sens. Environ.* 172, 50–66.
- Gattuso, J.-P., Gentili, B., Duarte, C.M., Kleypas, J.A., Middelburg, J.J., Antoine, D., 2006. Light availability in the coastal ocean: impact on the distribution of benthic photosynthetic organisms and their contribution to primary production. *Biogeosciences* 3, 489–513.
- Hakanson, L., Blenckner, T., 2008. A review on operational bioindicators for sustainable coastal management - criteria, motives and relationships. *Ocean Coast. Manag.* 51, 43–72.
- Harma, P., Vepsäläinen, J., Hannonen, T., Pyhälähti, T., Kamari, J., Kallio, K., Eloheimo, K., Koponen, S., 2001. Detection of water quality using simulated satellite data and semi-empirical algorithms in Finland. *Sci. Total Environ.* 268, 107–121.
- Harrington, J.A., Schiebe, F.R., Nix, J.F., 1992. Remote-sensing of Lake Chicot, Arkansas - monitoring suspended sediments, turbidity, and Secchi depth with Landsat MSS data. *Remote Sens. Environ.* 39, 15–27.
- He, X.Q., Pan, D.L., Bai, Y., Wang, T.Y., Chen, C.T.A., Zhu, Q.K., Hao, Z.Z., Gong, F., 2017. Recent changes of global ocean transparency observed by SeaWiFS. *Cont. Shelf Res.* 143, 159–166.
- He, M.J., He, S.Y., Zhang, X.D., Zhou, F., Li, P.L., 2021. Assessment of normalized water-leaving radiance derived from GOCI using AERONET-OC data. *Remote Sens.* 13, 1640.
- Holland, R.E., 1993. Changes in planktonic diatoms and water transparency in Hatchery Bay, Bass-Island area, Western Lake Erie since the establishment of the zebra mussel. *J. Gt. Lakes Res.* 19, 617–624.
- Hou, X., Feng, L., Duan, H., Chen, X., Sun, D., Shi, K., 2017. Fifteen-year monitoring of the turbidity dynamics in large lakes and reservoirs in the middle and lower basin of the Yangtze River, China. *Remote Sens. Environ.* 190, 107–121.
- Huang, J., Guo, L.J., Jiang, T., Zhu, H.C., 2019. Three decades of sea-ice variability in Jiaozhou Bay revealed by Landsat observations. *J. Ocean Univ. China* 18, 349–357.
- Ibrahim, A., Franz, B., Ahmad, Z., Healy, R., Knobelspiesse, K., Gao, B.-C., Proctor, C., Zhai, P.-W., 2018. Atmospheric correction for hyperspectral ocean color retrieval with application to the Hyperspectral imager for the Coastal Ocean (HICO). *Remote Sens. Environ.* 204, 60–75.
- Jia, H.L., Su, W., Huang, H.M., Sun, Q.Y., Jiang, G.J., Ma, R.H., 2018. Dynamic change characteristics and its dominant influencing factors of Secchi disk depth in coastal and inland waters. *Acta Opt. Sin.* 38, 0301001.
- Jiang, D.L., Matsushita, B., Setiawan, F., Vundo, A., 2019. An improved algorithm for estimating the Secchi disk depth from remote sensing data based on the new underwater visibility theory. *ISPRS J. Photogramm. Remote Sens.* 152, 13–23.
- Jing, L.D., Bai, S., Li, Y.H., Peng, Y., Wu, C.X., Liu, J.T., Liu, G.X., Xie, Z.C., Yu, G.L., 2019. Dredging project caused short-term positive effects on lake ecosystem health: a five-year follow-up study at the integrated lake ecosystem level. *Sci. Total Environ.* 686, 753–763.
- Joshi, I.D., D'Sa, E.J., 2018. An estuarine-tuned quasi-analytical algorithm (QAA-V): assessment and application to satellite estimates of SPM in Galveston Bay following hurricane Harvey. *Biogeosciences* 15, 4065–4086.
- Kim, S.H., Yang, C.S., Ouchi, K., 2015. Spatio-temporal patterns of Secchi depth in the waters around the Korean Peninsula using MODIS data. *Estuar. Coast. Shelf Sci.* 164, 172–182.
- Kirk, J.T.O., 1984. Dependence of relationship between inherent and apparent optical properties of water on solar altitude. *Limnol. Oceanogr.* 29, 350–356.
- Kukushkin, A.S., 2014. Long-term seasonal variability of water transparency in the surface layer of the deep part of the Black Sea. *Russ. Meteorol. Hydrol.* 39, 178–186.
- Lee, Z.P., Carder, K.L., Arnone, R.A., 2002. Deriving inherent optical properties from water color: a multiband quasi-analytical algorithm for optically deep waters. *Appl. Opt.* 41, 5755.
- Lee, Z.P., Du, K.P., Arnone, R., Liew, S., Bradley, 2005. Penetration of solar radiation in the upper ocean: a numerical model for oceanic and coastal waters. *J. Geophys. Res. Oceans* 110.
- Lee, Z.P., Lubac, B., Werdell, J., Arnone, R., 2009. An update of the quasi-analytical algorithm (QAA_v5). In: *International Ocean Color Group Software Report*, pp. 1–9.
- Lee, Z.P., Hu, C.M., Shang, S.L., Du, K.P., Lewis, M., Arnone, R., Brewin, R., 2013. Penetration of UV-visible solar radiation in the global oceans: insights from ocean color remote sensing. *J. Geophys. Res. Oceans* 118, 4241–4255.
- Lee, Z.P., Shang, S.L., Hu, C.M., Du, K.P., Weidemann, A., Hou, W.L., Lin, J.F., Lin, G., 2015. Secchi disk depth: a new theory and mechanistic model for underwater visibility. *Remote Sens. Environ.* 169, 139–149.
- Li, P., Li, G.X., Qiao, L.L., Chen, X., Shi, J.H., Gao, F., Wang, N., Yue, S.H., 2014. Modeling the tidal dynamic changes induced by the bridge in Jiaozhou Bay, Qingdao, China. *Cont. Shelf Res.* 84, 43–53.
- Li, H., He, X.Q., Shanmugam, P., Bai, Y., Wang, D.F., Huang, H.Q., Zhu, Q.K., Gong, F., 2019a. Radiometric sensitivity and signal detectability of ocean color satellite sensor under high solar zenith angles. *IEEE Trans. Geosci. Remote Sens.* 57, 8492–8505.
- Li, N., Shi, K., Zhang, Y.L., Gong, Z.J., Peng, K., Zhang, Y.B., Zha, Y., 2019b. Decline in transparency of Lake Hongze from long-term MODIS observations: possible causes and potential significance. *Remote Sens.* 11, 1777.
- Li, H., He, X.Q., Bai, Y., Shanmugam, P., Park, Y.-J., Liu, J., Zhu, Q.K., Gong, F., Wang, D. F., Huang, H.Q., 2020. Atmospheric correction of geostationary satellite ocean color data under high solar zenith angles in open oceans. *Remote Sens. Environ.* 249, 112022.
- Li, T., Zhu, B.Z., Cao, F., Sun, H., He, X.Q., Liu, M.L., Gong, F., Bai, Y., 2021. Monitoring changes in the transparency of the largest reservoir in eastern China in the past decade, 2013–2020. *Remote Sens.* 13, 2570.
- Liu, S.M., Zhang, J., Chen, H.T., Zhang, G.S., 2005. Factors influencing nutrient dynamics in the eutrophic Jiaozhou Bay, North China. *Prog. Oceanogr.* 66, 66–85.
- Liu, D., Duan, H.T., Loïsel, S., Hu, C.M., Zhang, G.Q., Li, J.L., Yang, H., Thompson, J.R., Cao, Z.G., Shen, M., Ma, R.H., Zhang, M., Han, W.X., 2020. Observations of water transparency in China's lakes from space. *Int. J. Appl. Earth Obs. Geoinf.* 92, 102187.
- Liu, C., Zhu, L.P., Li, J.S., Wang, J.B., Ju, J.T., Qiao, B.J., Ma, Q.F., Wang, S.L., 2021. The increasing water clarity of Tibetan lakes over last 20 years according to MODIS data. *Remote Sens. Environ.* 253, 112199.
- Lymburner, L., Botha, E., Hestir, E., Anstee, J., Sagar, S., Dekker, A., Malthus, T., 2016. Landsat 8: providing continuity and increased precision for measuring multi-decadal time series of total suspended matter. *Remote Sens. Environ.* 185, 108–118.
- Mao, Y., Wang, S.Q., Qiu, Z.F., Sun, D.Y., Bilal, M., 2018. Variations of transparency derived from GOCI in the Bohai Sea and the Yellow Sea. *Opt. Express* 26, 12191–12209.
- Menken, K.D., Brezonik, P.L., Bauer, M.E., 2006. Influence of chlorophyll and colored dissolved organic matter (CDOM) on lake reflectance spectra: implications for measuring lake properties by remote sensing. *Lake Reservoir Manag.* 22, 179–190.
- Mishra, S., Mishra, D.R., Lee, Z., 2014. Bio-optical inversion in highly turbid and cyanobacteria-dominated waters. *IEEE Trans. Geosci. Remote Sensing* 52, 375–388.
- Mobley, C.D., 1999. Estimation of the remote-sensing reflectance from above-surface measurements. *Appl. Opt.* 38, 7442–7455.
- Mueller, J., Fargion, G., McClain, C., Pegau, W., Zanefeld, J., Mitchell, B., Kahru, M., Wieland, J., Stramska, M., 2003. Ocean optics protocols for satellite ocean color sensor validation, Rev. 4. In: *Inherent Optical Properties: Instruments, Characterisations, Field Measurements And Data Analysis Protocols*, Vol. IV.
- Olmanson, L.G., Bauer, M.E., Brezonik, P.L., 2008. A 20-year Landsat water clarity census of Minnesota's 10,000 lakes. *Remote Sens. Environ.* 112, 4086–4097.
- Paerl, H.W., Valdes, L.M., Peierls, B.L., Adolf, J.E., Harding, L.J.W., 2006. Anthropogenic and climatic influences on the eutrophication of large estuarine ecosystems. *Limnol. Oceanogr.* 51, 448–462.
- Pardo-Pascual, J.E., Almonacid-Caballer, J., Ruiz, L.A., Palomar-Vázquez, J., 2012. Automatic extraction of shorelines from Landsat TM and ETM+ multi-temporal images with subpixel precision. *Remote Sens. Environ.* 123, 1–11.
- Pitarch, J., 2020. A review of Secchi's contribution to marine optics and the foundation of Secchi disk science. *Oceanography* 33, 26–37.
- Qing, S., Cui, T.W., Lai, Q., Bao, Y., Diao, R.X., Yue, Y.L., Hao, Y.L., 2021. Improving remote sensing retrieval of water clarity in complex coastal and inland waters with modified absorption estimation and optical water classification using Sentinel-2 MSI. *Int. J. Appl. Earth Obs. Geoinf.* 102, 102377.
- Ren, L., Zhang, M., Li, T., Zhu, C., Yang, J., 1999. Distribution of nutrients inside and outside Jiaozhou Bay. *J. Ocean Univ. Qingdao* 29, 692–698.
- Ren, J.L., Zheng, Z.B., Li, Y.M., Lv, G.N., Wang, Q., Lyu, H., Huang, C.C., Liu, G., Du, C. G., Mu, M., Lei, S.H., Bi, S., 2018. Remote observation of water clarity patterns in Three Gorges Reservoir and Dongting Lake of China and their probable linkage to the Three Gorges Dam based on Landsat 8 imagery. *Sci. Total Environ.* 625, 1554–1566.
- Ritchie, J.C., Cooper, C.M., Schiebe, F.R., 1990. The relationship of MSS and TM digital data with suspended sediments, chlorophyll, and temperature in Moon Lake, Mississippi. *Remote Sens. Environ.* 33, 137–148.
- Ruddick, K.G., Ovidio, F., Rijkeboer, M., 2000. Atmospheric correction of SeaWiFS imagery for turbid coastal and inland waters. *Appl. Opt.* 39, 897–912.
- Shang, Y.X., Liu, G., Wen, Z.D., Jacinthe, P.A., Song, K.S., Zhang, B., Lyu, L.L., Li, S.J., Wang, X., Yu, X.F., 2021. Remote estimates of CDOM using Sentinel-2 remote sensing data in reservoirs with different trophic states across China. *J. Environ. Manag.* 286, 112275.
- Shanmugam, P., Sundarabalan, B., Ahn, Y.H., Ryu, J.H., 2011. A new inversion model to retrieve the particulate backscattering in coastal/ocean waters. *IEEE Trans. Geosci. Remote Sens.* 49, 2463–2475.
- Shen, M., Duan, H.T., Cao, Z.G., Xue, K., Qi, T.C., Ma, J.G., Liu, D., Song, K.S., Huang, C. L., Song, X.Y., 2020. Sentinel-3 OLCI observations of water clarity in large lakes in eastern China: implications for SDG 6.3.2 evaluation. *Remote Sens. Environ.* 247, 111950.
- Shi, W., Wang, M.H., Jiang, L.D., 2011. Spring-neap tidal effects on satellite ocean color observations in the Bohai Sea, Yellow Sea, and East China Sea. *J. Geophys. Res. Oceans* 116, C12032.
- Shi, K., Zhang, Y.L., Zhu, G.W., Qin, B.Q., Pan, D.L., 2018. Deteriorating water clarity in shallow waters: evidence from long term MODIS and in-situ observations. *Int. J. Appl. Earth Obs. Geoinf.* 68, 287–297.

- Song, Z.J., Gong, L.M., Chen, Q., Gu, Z.K., Gao, L., Huang, H.J., 2015. Influence on the environment of the coastal area in Jiaozhou Bay of China. *Environ. Eng. Manag. J.* 14, 1897–1903.
- Song, K.S., Liu, G., Wang, Q., Wen, Z.D., Lyu, L.L., Du, Y.X., Sha, L.W., Fang, C., 2020. Quantification of lake clarity in China using Landsat OLI imagery data. *Remote Sens. Environ.* 243, 111800.
- Sun, D.Y., Li, Y.M., Wang, Q., Le, C.F., Huang, C.C., Wang, L.Z., 2009. Parameterization of water component absorption in an inland eutrophic lake and its seasonal variability: a case study in Lake Taihu. *Int. J. Remote Sens.* 30, 3549–3571.
- Sun, D.Y., Li, Y.M., Wang, Q., Lv, H., Le, C.F., Huang, C.C., Gong, S.Q., 2010. Partitioning particulate scattering and absorption into contributions of phytoplankton and non-algal particles in winter in Lake Taihu (China). *Hydrobiologia* 644, 337–349.
- Sun, L., Jiang, J.G., Zhu, W.N., 2017. Remote sensing inversion and daily variation of CDOM based on GOCI in the Changjiang Estuary and adjacent water. *Haiyang Xuebao* 39, 133–145.
- Taillie, D.M., O'Neil, J.M., Dennison, W.C., 2020. Water quality gradients and trends in New York Harbor. *Reg. Stud. Mar. Sci.* 33, 100922.
- Testa, J.M., Lyubchich, V., Zhang, Q., 2019. Patterns and trends in Secchi disk depth over three decades in the Chesapeake Bay estuarine complex. *Estuar. Coasts* 42, 927–943.
- Tilzer, M.M., 1988. Secchi disk — chlorophyll relationships in a lake with highly variable phytoplankton biomass. *Hydrobiologia* 162, 163–171.
- Wang, Q.M., Atkinson, P.M., 2018. Spatio-temporal fusion for daily Sentinel-2 images. *Remote Sens. Environ.* 204, 31–42.
- Wang, S.L., Li, J.S., Zhang, B., Lee, Z., Spyarakos, E., Feng, L., Liu, C., Zhao, H.L., Wu, Y. H., Zhu, L.P., Jia, L.M., Wan, W., Zhang, F.F., Shen, Q., Tyler, A.N., Zhang, X.F., 2020. Changes of water clarity in large lakes and reservoirs across China observed from long-term MODIS. *Remote Sens. Environ.* 247, 111949.
- Wu, G.F., de Leeuw, J., Liu, Y.L., 2009. Understanding seasonal water clarity dynamics of Lake Dahuchi from in situ and remote sensing data. *Water Resour. Manag.* 23, 1849–1861.
- Xiao, Y.J., Ferrerira, J.G., Bricker, S.B., Nunes, J.P., Zhu, M.Y., Zhang, X.L., 2007. Trophic assessment in Chinese coastal systems - review of methods and application to the Changjiang (Yangtze) Estuary and Jiaozhou Bay. *Estuar. Coasts* 30, 901–918.
- Yin, Z.Y., Li, J.S., Huang, J., Wang, S.L., Zhang, F.F., Zhang, B., 2021a. Steady increase in water clarity in Jiaozhou Bay in the Yellow Sea from 2000 to 2018: observations from MODIS. *J. Oceanol. Limnol.* 39, 14.
- Yin, Z.Y., Li, J.S., Liu, Y., Xie, Y., Zhang, F.F., Wang, S.L., Sun, X., Zhang, B., 2021b. Water clarity changes in Lake Taihu over 36 years based on Landsat TM and OLI observations. *Int. J. Appl. Earth Obs. Geoinf.* 102, 102457.
- Yu, X.L., Lee, Z.P., Shen, F., Wang, M.H., Wei, J.W., Jiang, L.D., Shang, Z.H., 2019. An empirical algorithm to seamlessly retrieve the concentration of suspended particulate matter from water color across ocean to turbid river mouths. *Remote Sens. Environ.* 235, 111491.
- Zeng, S., Lei, S.H., Li, Y.M., Lyu, H., Xu, J.F., Dong, X.Z., Wang, R., Yang, Z.Q., Li, J.C., 2020. Retrieval of Secchi disk depth in turbid lakes from GOCI based on a new semi-analytical algorithm. *Remote Sens.* 12, 1516.
- Zhang, Y.L., Wu, Z.X., Liu, M.L., He, J.B., Shi, K., Wang, M.Z., Yu, Z.M., 2014. Thermal structure and response to long-term climatic changes in Lake Qiandaohu, a deep subtropical reservoir in China. *Limnol. Oceanogr.* 59, 1193–1202.
- Zhang, Y.L., Qin, B.Q., Zhu, G.W., Shi, K., Zhou, Y.Q., 2018. Profound changes in the physical environment of Lake Taihu from 25 years of long-term observations: implications for algal bloom outbreaks and aquatic macrophyte loss. *Water Resour. Res.* 54, 4319–4331.
- Zhang, K., Jiang, T., Huang, J., 2019. Spatial-temporal variation in sea surface temperature from Landsat time series data using annual temperature cycle. *J. Coast. Res.* 58–65.
- Zhang, Y.B., Shi, K., Zhang, Y.L., Moreno-Madrián, M.J., Xu, X., Zhou, Y.Q., Qin, B.Q., Zhu, G.W., Jeppesen, E., 2021. Water clarity response to climate warming and wetting of the Inner Mongolia-Xinjiang Plateau: a remote sensing approach. *Sci. Total Environ.* 796, 148916.
- Zhao, D.H., Cai, Y., Jiang, H., Xu, D.L., Zhang, W.G., An, S.Q., 2011. Estimation of water clarity in Taihu Lake and surrounding rivers using Landsat imagery. *Adv. Water Resour.* 34, 165–173.
- Zhao, K., Qiao, L., Shi, J., He, S., Li, G., Yin, P., 2015. Evolution of sedimentary dynamic environment in the western Jiaozhou Bay, Qingdao, China in the last 30 years. *Estuar. Coast. Shelf Sci.* 163, 244–253.
- Zhao, Y.L., Wang, S.L., Zhang, F.F., Shen, Q., Li, J.S., 2021. Retrieval and spatio-temporal variations analysis of Yangtze River water clarity from 2017 to 2020 based on Sentinel-2 images. *Remote Sens.* 13, 22.
- Zhou, Q.C., Wang, W.L., Huang, L.C., Zhang, Y.L., Qin, J., Li, K.D., Chen, L., 2019. Spatial and temporal variability in water transparency in Yunnan Plateau lakes, China. *Aquat. Sci.* 81, 36.